

Daily to centennial behavior of aseismic slip along the central section of the North Anatolian Fault

R. Jolivet^{1,2}, J. Jara¹, M. Dalaison¹, B. Rouet-Leduc³, A. Özdemir⁴, U.
Dogan⁴, Z. Çakir⁵, S. Ergintav⁶ & P. Dubernet¹

¹Laboratoire de Géologie, Département de Géosciences, École Normale Supérieure, PSL Université, CNRS
UMR 8538, Paris, France

²Institut Universitaire de France, 1 rue Descartes, 75006 Paris

³Disaster Prevention Research Institute, Kyoto University, Kyoto, Japan

⁴Department of Geomatic Engineering, Yildiz Technical University, 34220 Istanbul, Turkey

⁵Department of Geology, Istanbul Technical University, 34469 Istanbul, Turkey

⁶Department of Geodesy, Kandilli Observatory and Earthquake Research Institute, Bogazici University,
34684 Istanbul, Turkey

Key Points:

- We image the spatio-temporal variations of aseismic slip along the central section of the North Anatolian Fault with InSAR and GNSS data
- Slow slip extends over 70 km, reaches 1 cm/yr and coincides with shallow locking depth along the fault
- Slow slip events do not occur along the whole creeping section but have been detected since, at least, the 1980's

Corresponding author: Romain Jolivet, romain.jolivet@ens.fr

Abstract

20 Slow, aseismic slip plays a crucial role in the initiation, propagation and arrest of large
21 earthquakes along active faults. In addition, aseismic slip controls the budget of elas-
22 tic strain in the crust, hence the amount of energy available for upcoming earthquakes.
23 The conditions for slow slip include specific material properties of the fault zone, pore
24 fluid pressure and geometrical complexities of the fault plane. Fine scale descriptions of
25 aseismic slip at the surface and at depth are key to determine the factors controlling the
26 occurrence of slow, aseismic versus rapid, seismic fault slip. We focus on the spatial and
27 temporal distribution of aseismic slip along the North Anatolian Fault, the plate bound-
28 ary accommodating the 2 cm/yr of relative motion between Anatolia and Eurasia. Along
29 the eastern termination of the rupture trace of the 1944 M7.3 Bolu-Gerede earthquake
30 lies a segment that slips aseismically since at least the 1950's. We use Sentinel 1 time
31 series of displacement and GNSS data to provide a spatio-temporal description of the
32 kinematics of fault slip. We show that aseismic slip observed at the surface is coincident
33 with a shallow locking depth and that slow slip events with a return period of 2.5 years
34 are restricted to a specific section of the fault. In the light of historical measurements,
35 we discuss potential rheological implications of our results and propose a simple alter-
36 native model to explain the local occurrence of shallow aseismic slip at this location.
37

38 Plain Language Summary

39 Earthquakes are the manifestation of the rapid release of elastic energy stored in
40 the crust under the action of moving tectonic plates on either sides of a fault system. In-
41 terestingly, some faults release energy under the form of aseismic slip, which is slow and
42 harmless. The conditions for slow slip, as opposed to earthquakes, are not fully under-
43 stood and it appears of higher importance to study high-resolution, small scale features
44 to grow our understanding. We analyze satellite Radar imagery and GNSS data to build
45 a movie of ground motion in the vicinity of the North Anatolian Fault in Turkey over
46 a section that was recognized to slip aseismically in the 70's. We show that aseismic slip
47 there is made of slow slip events repeating every 2.5 years embedded within a larger re-
48 gion that slips steadily. Using these data, we model the distribution of slip rates at depth
49 on the fault and show that aseismic slip extends until 5-8 km depth. Below, the fault
50 is locked, accumulating energy for upcoming earthquakes. In the light of past measure-
51 ments and based on our high-resolution dataset, we discuss potential physical models
52 explaining the occurrence of slow slip in this region.

53 1 Introduction

54 The discovery of slow, aseismic slip in the 1960's both along the San Andreas Fault
 55 (Steinbrugge et al., 1960) and the North Anatolian Fault (Ambraseys, 1970) led to a re-
 56 vision of the elastic rebound theory proposed by Reid (1911). Slow slip has now been
 57 described along numerous active faults, including the San Andreas Fault (e.g. Steinbrugge
 58 et al., 1960; Jolivet, Simons, et al., 2015), the North Anatolian Fault (e.g. Ambraseys,
 59 1970; Çakir et al., 2005), the Leyte fault (e.g. Duquesnoy et al., 1994; Dianala et al., 2020)
 60 among others (see a complete description in Jolivet and Frank (2020)), and is now rec-
 61 ognized as one end-member mode of fault slip releasing stress along active faults. Slow
 62 slip has also been described along subduction megathrust either in the form of transient
 63 events (e.g. Dragert et al., 2001; Wallace, 2020), associated with tremors or not, and as
 64 variations of megathrust kinematic coupling (e.g. Mazzotti et al., 2000; Avouac, 2015).
 65 Observationally, slow slip has been linked with the preparation phase of earthquakes, such
 66 as before the M_w 8.1 Iquique earthquake in Chile in 2014 (e.g. Ruiz et al., 2014; Socquet
 67 et al., 2017) or, more disputably, before the M_w 7.4 Izmit earthquake in 1999 in Turkey
 68 (Bouchon et al., 2011; Ellsworth & Bulut, 2018). Effectively, slow slip, like earthquakes,
 69 contributes to the release of elastic energy that accumulates under the loading imposed
 70 by tectonic motion (e.g. Avouac, 2015). As a result, slow slip influences the size of large
 71 earthquakes which are known to be arrested preferentially by fault segments hosting aseis-
 72 mic slip (e.g. Kaneko et al., 2010), among other causes.

73 Although the importance of aseismic slip on the dynamics of earthquakes is indis-
 74 putable (e.g. Avouac, 2015; Bürgmann, 2018), the physical mechanisms responsible for
 75 keeping slip slow are still unclear. Multiple mechanisms may be involved to prevent fault
 76 slip to become dynamic and reach slip speeds characteristic of earthquakes (~ 1 m/s).
 77 First, the spatial distribution of rheological properties of the fault material governs the
 78 spatial and temporal evolution of fault slip. For instance, rate strengthening fault ma-
 79 terial leads to stable slip (e.g. Scholz, 1998; Thomas et al., 2017). As fault rheology, and
 80 in particular the constitutive properties of the law controlling friction on the fault plane,
 81 depends on temperature and normal stress, the resulting depth-dependent distribution
 82 of fault properties explains the depth distribution of slip modes in a variety of subduc-
 83 tion zones and continental faults (e.g. Blanpied et al., 1991; den Hartog & Spiers, 2013).
 84 Second, if fault frictional properties lead to a rate weakening behavior, a large nucleation
 85 size (i.e. the slip distance over which slip becomes dynamic) may prevent slip to reach

86 seismic speeds (e.g. Ampuero & Rubin, 2008). As nucleation size depends on both con-
87 stitutive properties and effective normal stress, one may invoke the influence of elevated
88 pore fluid pressure to keep slip stable, as observed at the deep end of the potentially seis-
89 mogenic portion of subduction megathrust (e.g. Kodaira et al., 2004; Moreno et al., 2014).
90 Third, recent works suggest that complexities in the fault geometry may lead to the emer-
91 gence of slow slip even with unstable rate-weakening properties, either through local mod-
92 ulation of normal stress due to slip on a rough fault (Cattania & Segall, 2021) or to stress
93 interactions between fault segments (Romanet et al., 2018). In all cases, it is important
94 to realize that the geological conditions underlying these physical mechanisms may vary
95 over a wide range of length scales. Rock types, pore fluid pressure and fault geometry
96 may vary over any distances, from millimeters to hundreds of kilometers. Fault geom-
97 etry for instance is considered self-similar and has no characteristic length scale (e.g. Can-
98 dela et al., 2012).

99 It is therefore of uttermost importance to provide descriptions of aseismic, slow slip
100 with the highest level of details over large regions. In subduction zones, the vast major-
101 ity of geodetic and seismological stations are necessarily located on land, far from the
102 megathrust. To the contrary, the surface expression of continental faults can be stud-
103 ied with high levels of detail due to available Interferometric Synthetic Aperture Radar
104 (InSAR) data, near-field GNSS stations and creepmeters, which may reveal the small-
105 est details of aseismic slip. For instance, Jolivet, Candela, et al. (2015) and Khoshmanesh
106 and Shirzaei (2018) have explored the occurrence of clusters of slow slip events with scales
107 from tens of meters to tens of kilometers, suggesting an avalanche-like behavior witness-
108 ing interactions between slow slip events. As another example, Dalaison et al. (2021) show
109 the complex pattern of slow and rapid slip along the Chaman fault in Pakistan which
110 hosts one of the longest creeping sections on Earth. In this paper, we explore and de-
111 scribe the behavior of aseismic slip along the Ismetpasa section of the North Anatolian
112 Fault (Fig. 1), covering time scales ranging from days to decades and length scales from
113 hundreds of meters to tens of kilometers.

114 **2 Seismo-tectonic setting and motivation**

115 First mentions of aseismic slip along the North Anatolian Fault date from Ambraseys
116 (1970). In particular, Ambraseys (1970) describes the offset of a wall in the city of Is-
117 metpasa which was not related to any significant seismic activity. Although the paper

118 mentions that it is not known whether the offset occurred gradually or episodically, a
119 mean creep rate of 2 cm/yr was inferred while the earlier offset of railroad tracks in the
120 vicinity suggested a 5 cm/yr creep rate from 1944 to 1950. Following the suggestion of
121 Ambraseys (1970), Bilham et al. (2016) re-evaluated these surface slip rates, inferring
122 slightly slower rates. The 1944 M 7.4 Gerede earthquake is the last large event known
123 to have ruptured in this area, and those early estimates fall within the subsequent post-
124 seismic period (e.g. Fig. 1 and Kondo et al., 2010). Since then, numerous studies have
125 measured surface slip rates, using land-based and geodetic techniques, including creep-
126 meters, GNSS data and InSAR data (Aytun, 1982; Eren, 1984; Deniz et al., 1993; Al-
127 tay & Sav, 1991; Çakir et al., 2005; Kutoglu & Akcin, 2006; Kutoglu et al., 2008, 2010;
128 Karabacak et al., 2011; Deguchi, 2011; Kaneko et al., 2012; Ozener et al., 2013; Cetin
129 et al., 2014; Bilham et al., 2016). All subsequent studies infer a surface creep rate, at Is-
130 metpasa, of about 6 to 8 mm/yr, since at least the 1980's. The decrease in slip rate from
131 5 cm/yr followed by a rather constant rate of 6 to 8 mm/yr was interpreted as the sig-
132 nature of a long lived post-seismic signal and modeled with rate-and-state friction (Kaneko
133 et al., 2012). The model suggests that shallow material, from the surface to a depth of
134 about 5 km, is rate-strengthening, promoting shallow afterslip. Prompting adequate tun-
135 ing of the constitutive parameters of the friction law, this model can produce long lived
136 afterslip lasting more than 55 years. It is important to realize that all these measure-
137 ments were made and restricted to a single location along the fault and that the slip rates
138 measured directly following the 1944 earthquake are uncertain (Bilham et al., 2016).

139 Slow slip events were recently discovered at Ismetpasa (Bilham et al., 2016; Rous-
140 set et al., 2016). In 2013, a 2 cm slow slip event was detected from time series analysis
141 of InSAR data acquired by the Cosmo-Skymed constellation (Rousset et al., 2016). Slip
142 spanned a 10 km-long section of the fault with a 4 km width along dip. Such event echoes
143 the surface slip accelerations inferred from creepmeter records in the 1980's (Altay & Sav,
144 1991) and those currently captured by the creepmeter operating since 2014 (Bilham et
145 al., 2016). The largest slow slip events are spontaneous as they do not follow significant
146 earthquakes or identified stress perturbation. They repeat every 2 to 3 years with slip
147 amplitudes that vary from 5 to 15 mm. These events were not accounted for as such in
148 early measurements of surface slip rates (e.g. Altay & Sav, 1991) and are most likely av-
149 eraged into such rates. In addition, we do not know the full spatial extent of these slow
150 slip events. Finally, the presence of such events suggests that the rheology of the fault

151 at shallow depth cannot be uniformly rate-strengthening and two possibilities arise. Rhe-
152 ology is either rate-weakening, hence promoting spontaneous slip instabilities although
153 such instabilities must remain slow, or rheology is heterogeneous with unstable fault patches
154 embedded in a generally stable matrix (Wei et al., 2013).

155 In all cases, several questions are left unanswered considering the slip rate varia-
156 tions and distribution along the creeping section of Ismetpasa. First, although the spa-
157 tial distribution of slip has already been inferred (Cetin et al., 2014), it is unclear how
158 deep slip extends and what are the uncertainties associated with the slip distribution.
159 Large scale strain mapping and modeling are not sufficient and fine exploration of the
160 deformation field in this area is required (Weiss et al., 2020; Barbot & Weiss, 2021). Sec-
161 ond, temporal variations of slip rate have, so far, only been detected at Ismetpasa. Is
162 such episodic behavior representative of the whole fault section or not?

163 To address these questions, we derive time series of surface displacements over the
164 2014-2021 period from Sentinel 1 InSAR data and explore the spatial and temporal be-
165 havior of aseismic slip along this creeping section. We also include ground velocity mea-
166 sured at GNSS sites from the National Turkish network and preliminary results from a
167 network of near-fault GNSS sites designed to capture slow slip events. In the following,
168 after specifying our approach, we describe the resulting surface velocity field and infer
169 the distribution of average slip rates at depth along with associated uncertainties. We
170 then explore potential surface slip rate variations to detect small slow slip events over
171 the whole extent of the creeping section. We finally discuss the occurrences of such slow
172 events in the light of previously measured surface slip rates and elaborate on the rhe-
173 ology of the fault zone.

174 **3 Data processing**

175 **3.1 InSAR data processing**

176 We process all available Synthetic Aperture Radar data from the Sentinel 1 con-
177 stellation from 2014 to late 2020 with the ISCE processing environment (JPL/Caltech,
178 winsar.unavco.org/isce.html; Gurrola et al., 2010) using the same approach as Dalaison
179 et al. (2021). We process data from descending tracks 65 and 167 and ascending track
180 87. First, we coregister all images to a single reference acquisition chosen in the middle
181 of the time series of images. Coregistration is performed using satellite orbits and refined

182 using the spectral diversity available on Radar burst overlaps (Fattahi et al., 2016). From
 183 the 288, 278 and 293 acquisitions on tracks 65, 167 and 87 respectively, we then com-
 184 pute 1858, 1826 and 3053 interferograms (see supplementary figures S-1 to S-3 for base-
 185 line plots). We remove the contribution of the stratified tropospheric delay from the wrapped
 186 interferograms using the ERA5 re-analysed temperature, water vapor and pressure level
 187 heights fields (Jolivet et al., 2011, 2014) using the PyAPS software (Agram et al., 2013).
 188 We look down interferograms for a final pixel size of about 120 m in azimuth and range
 189 direction (i.e. 8 looks in azimuth and 32 looks in range). We then filter and unwrap in-
 190 terferograms using the adaptive phase filter and the coherence-based branch cut algo-
 191 rithm available in ISCE (Goldstein et al., 1988; Goldstein & Werner, 1998). We finally
 192 correct for potential unwrapping errors using the CorPhu algorithm (Benoit et al., 2020).
 193 Independently on each track, we use the Kalman filter approach developed by Dalaison
 194 and Jolivet (2020) to reconstruct the time series of surface displacements in the satel-
 195 lite Line-Of-Sight (hereafter LOS) from the set of interferograms. Since no significant
 196 earthquake has been detected in the region over the period we analyse, we only consider
 197 an annual oscillation and a secular trend as a basis model underlying the Kalman filter.
 198 We use the parameterization proposed in Dalaison and Jolivet (2020).

199 Results are shown on Fig. 1 and S-4 to S-15 of the supplementary informations.
 200 As interferograms do not unwrap completely, with especially poor coherence in the north
 201 of the area close to the shore of the Black Sea, final reconstruction of the time series shows
 202 variable quality. We define the reconstruction Root Mean Square (RMS) as the square
 203 root of the sum of the squared difference between the interferograms and the synthetic
 204 interferograms inferred from our time series, divided by the total number of interfero-
 205 grams. We compute such RMS for each pixel of each track (Figures S-13 to S-15 of the
 206 supplementary informations). We decide to mask pixels with a reconstruction RMS higher
 207 than 2 mm, pixels constrained by less than 1300 interferograms (Figures S-10 to S-12
 208 of the supplementary informations) and with a final uncertainty on the velocity higher
 209 than 0.5 mm/yr (Figures S-7 to S-9 of the supplementary informations). We retain for
 210 the following analysis pixels less than 60 km away from the North Anatolian Fault trace.
 211 We combine the final three LOS velocity maps into fault parallel and vertical velocity
 212 maps assuming horizontal motion aligns with 77.5°N azimuth (Dalaison et al., 2023). Fi-
 213 nal horizontal velocity is shown on Fig. 1 while the vertical velocity map is available on
 214 Fig. S-18 of the supplementary materials.

215 Similar to Dalaison et al. (2021), we extract fault perpendicular profiles on each
 216 LOS velocity maps every 250 m and evaluate the across fault ground velocity difference
 217 to infer the surface slip rate and the associated uncertainties (Fig. S-16 and Fig. S-17
 218 of the supplementary materials). Such slip rate is remarkably consistent between both
 219 descending tracks 65 and 167 and shows opposite sign on track 87, suggesting a dom-
 220 inantly strike slip motion across the fault. We combine these along strike surface slip mea-
 221 surements into a strike slip and dip slip motion (Fig. 1 and Fig. S-17 of the supplemen-
 222 tary materials). Potential dip slip is visible between 32.5° and 32.75° W of longitude, near
 223 Ismetpasa.

224 3.2 GNSS data processing

225 We installed 19 permanent GNSS sites along the section previously identified as
 226 creeping by Cetin et al. (2014). Sites are located close to the fault (< 5 km) in order
 227 to capture shallow slow slip events, previously captured with InSAR and creepmeter data
 228 (Altay & Sav, 1991; Bilham et al., 2016; Rousset et al., 2016). In this paper, we only seek
 229 to include velocities measured at each site of this network, hereafter referred to as Is-
 230 menet, to constrain the slip rate at shallow depths. A detailed description of the typ-
 231 ical site setup we implemented with station measurement periods can be found in the
 232 supplementary informations. We processed data from the Ismenet network together with
 233 57 stations from the International GNSS service (37 sites, www.igs.org) and from the
 234 Turkish National Network (20 sites, <https://www.tusaga-aktif.gov.tr/>). A detailed
 235 description of the sites used can be found in supplementary materials.

236 Observations are processed in double differences using the GAMIT/GLOBK 10.7
 237 software (Herring et al., 2018) to obtain daily estimates of station positions, choosing
 238 ionosphere-free combination and fixing the ambiguities to integer values. We use pre-
 239 cise orbits from the International GNSS Service for Geodynamics, precise EOPs from
 240 the IERS bulletin B, IGS tables to describe the phase centers of the antennas, FES2004
 241 ocean-tidal loading corrections, and atmospheric loading corrections (tidal and non-tidal).
 242 One tropospheric vertical delay parameter and two horizontal gradients per stations are
 243 estimated every 2 hours. We use the GLOBK software (Herring et al., 2015) to combine
 244 daily solutions and the PYACS software (Nocquet, 2018a) to derive the position time
 245 series, which are then mapped into the ITRF 2014 reference frame (Altamimi et al., 2016).
 246 Finally, the time series are set in a fixed Eurasian frame, considering the pole solution

247 proposed by Altamimi et al. (2016). We use a trajectory model to extract the velocity
 248 on each time series (Bevis & Brown, 2014) and evaluate the standard deviation on ve-
 249 locities assuming white and flicker noise following Williams (2003).

250 4 Surface velocity and average slip rate

251 4.1 Surface velocity across the North Anatolian Fault

252 Our velocity map is consistent with previously published results (e.g. Kaneko et
 253 al., 2012; Cetin et al., 2014). Although decoherence and poor RMS reconstruction leaves
 254 gaps in the velocity map, we clearly identify the signature of the North Anatolian Fault
 255 with a gradient of ~ 2 cm/yr across the fault which varies significantly along strike (Fig.
 256 1, 2 and S-16). Along most portions of the fault, the across fault gradient of displace-
 257 ment rate is gradual with a 20-30 km-wide transition from westward to eastward mo-
 258 tion (i.e. west of 32.4°E and east of 33.4°E).

259 Between 32.4°E and 33.4°E , we observe a very sharp, step-like gradient of veloc-
 260 ity across the fault both in the InSAR-derived fault parallel velocity map and in the GNSS-
 261 derived velocities (Fig. 1 and 2). We interpret this step-like transition as the signature
 262 of surface slip over an approximately 60 to 70 km-long profile. This surface slip rate shows
 263 a maximum slip rate of 1 ± 0.2 cm/yr that tappers down laterally to negligible values in
 264 an almost elliptical shape. Slip rate at the city of Ismetpasa (longitude 32.63°E) is $6\pm$
 265 2 mm/yr, consistent with published rates from creepmeter measurements (Bilham et al.,
 266 2016). Uncertainties are on the order of 2 to 3 mm/yr. The distribution of slip at the
 267 surface overlaps with both the eastern termination of the 1944 Bolu-Gerede ($M_w 7.4$) earth-
 268 quake and the western end of the 1943 Tosya ($M_w 7.6$) earthquake (Kondo et al., 2005;
 269 Barka, 1996). This segment also overlaps with the rupture of the 1951 Kursunlu $M_w 6.9$
 270 earthquake, although the extent of that rupture is unclear (Ambraseys, 1970; Barka, 1996).

271 We observe significant vertical differential motion across the fault near the city of
 272 Ismetpasa, where the northern block subsides with respect to the southern block (Fig.
 273 1). The rate of vertical differential motion reaches locally 12 ± 3 mm/yr but its extent
 274 does not exceed 15 km along strike. We also observe pronounced subsidence north of the
 275 fault, with a maximum of 10 mm/yr, over a 15 km-wide region bounded by the trace of
 276 the North Anatolian Fault to the south (Fig. 1). We account for this subsidence signal
 277 in further modeling in order not to bias slip rate estimates at depth. This subsidence sig-

278 nal overlaps with cultivated land, suggesting potential hydrological effects related to wa-
 279 ter pumping. Other signals of vertical motion can be observed in various places in the
 280 velocity map but further away from the fault (> 20 km), hence these should average out
 281 in the data decimation process and not affect our model inference. We do not observe
 282 any other subsidence signal along the fault trace. Finally, we raise the readers' atten-
 283 tion to the fact that such subsidence is observed where previous local measurements of
 284 aseismic slip were done.

285 4.2 Slip distribution and uncertainties

286 The surface velocity field described above is consistent with strain localizing in the
 287 vicinity of a major strike slip, plate boundary fault. We do not observe significant sig-
 288 nals associated with other faults, hence we assume surface displacement rates originate
 289 from slip along the North Anatolian Fault at depth. Following the approach of Jolivet,
 290 Simons, et al. (2015), we consider the NAF as a vertical fault embedded in an elastic crust.
 291 Surface displacement resulting from elastic loading is usually modeled as the result of
 292 slip on an infinitely deep dislocation buried below a given locking depth (Savage & Bur-
 293 ford, 1973). Aseismic slip can be modeled as the result of shallow elastic dislocations (e.g
 294 Ryder & Bürgmann, 2008; Maurer & Johnson, 2014; Jolivet, Simons, et al., 2015; Bletery
 295 et al., 2020). Finally, local subsidence can be modeled using an *ad hoc* Mogi source with
 296 a pressure or volume change (Mogi, 1958).

297 We model the surface displacement captured by the three InSAR line-of-sight ve-
 298 locity maps and by our local GNSS network as the sum of 4 contributions. Note that,
 299 here, we do not use the horizontal and vertical motion maps but directly the LOS ve-
 300 locity maps. First, we solve for strike slip rate on infinitely deep dislocations following
 301 the trace of the NAF buried below 20-km-depth. This depth is chosen deep enough to
 302 reach the brittle-ductile transition and to allow shallower slip on the shallow portion of
 303 the NAF in case the effective locking depth is located above 20-km-depth. Second, we
 304 discretize the NAF fault plane above the locking depth up to the surface in a triangu-
 305 lar mesh. Slip on this fault plane is the linear interpolation of slip values at each node
 306 of the triangular mesh. Triangle sizes vary from 1 km at the surface to 10 km at depth
 307 (see supplementary informations Fig. S-29). Third, we model local vertical motion across
 308 the NAF at Ismetpasa by dip slip motion on a subset of the mesh used for strike slip.
 309 For all fault models, we compute Green's functions relating slip to surface displacements

310 in a semi-infinite stratified half-space using the stratification of elastic parameters from
 311 Rousset et al. (2016). Fourth, we include a Mogi source at an arbitrary depth of 3 km
 312 below the subsiding basin north of Ismetpasa (Mogi, 1958). We include this source to
 313 remove the potential bias on the inferred strike slip rate. We are not interested in the
 314 actual values of pressure change in the source which tradeoff with its depth and size, hence
 315 the arbitrary choice of the depth of the source.

316 In addition, we model long wavelength signals in each InSAR velocity maps (i.e.
 317 orbital errors, long wavelength atmospheric signals, etc) as a linear function of longitude
 318 and latitude. We also solve for a translation and a rotation within the GNSS velocity
 319 field. These geometrical transformations allow to place the data in a reference frame in
 320 which displacement rates are null on top of the fault, consistently with our setup. Fi-
 321 nal parameter set includes slip rate on deep dislocations to model crustal elastic load-
 322 ing, slip rate on the shallow, discretized NAF, dip slip in the vicinity of Ismetpasa, a Mogi
 323 source north of Ismetpasa and geometric parameters for InSAR and GNSS common ref-
 324 erencing.

325 We downsample the InSAR velocity maps to minimize computational burden us-
 326 ing a quadtree approach designed to maximize resolution on the fault plane (Lohman
 327 & Simons, 2005; Jolivet, Simons, et al., 2015). In order to avoid averaging velocities across
 328 the fault, we exclude pixels located less than 1 km from the fault trace. Doing so, we lose
 329 precious information on potential slip along the shallowest portion of the fault (< 1 km-
 330 depth). We therefore model the across fault step measured in the three LOS velocity maps
 331 and we force slip to be constant between the surface and a depth of 1 km. Moreover, to
 332 ensure continuity of slip rates at depth, we constrain slip rates along the deepest elements
 333 of the meshed NAF to equal those along the deep dislocations.

334 We explore the range of possible models using a Bayesian approach in order to de-
 335 rive the posterior Probability Density Function of models. Effectively, the posterior PDF,
 336 $\Theta(\mathbf{m}|\mathbf{d})$, is proportional to the product of the prior PDF (i.e. our state of knowledge be-
 337 fore considering any data), $\rho(\mathbf{m})$, with the likelihood (i.e. the probability that a model
 338 will lead to a prediction that fits the data), $L(\mathbf{d}|\mathbf{m})$, according to Bayes' theorem, such
 339 as

$$\Theta(\mathbf{m}|\mathbf{d}) \propto \rho(\mathbf{m})L(\mathbf{d}|\mathbf{m}), \quad (1)$$

340 where \mathbf{m} is the vector of model parameters and \mathbf{d} is the data vector. As a prior PDF,
 341 we consider a uniform distribution from 0 to 50 mm/yr for strike slip on the shallow part
 342 of the NAF. Since most plate reconstruction models suggest a long term slip rate of the
 343 NAF around 20 mm/yr (e.g. DeMets et al., 2010), we consider a uniform distribution
 344 between 10 and 30 mm/yr for the deep dislocations. We consider uniform distributions
 345 for the parameters of the geometric transformations applied to each of the geodetic datasets.
 346 We chose a Gaussian formulation for the likelihood such as

$$L(\mathbf{d}|\mathbf{m}) \propto \exp -\frac{1}{2}(\mathbf{G}\mathbf{m} - \mathbf{d})^T \mathbf{C}_\chi^{-1}(\mathbf{G}\mathbf{m} - \mathbf{d}), \quad (2)$$

347 where \mathbf{G} is the matrix of Green’s functions. Following the approach of Duputel et al. (2014),
 348 \mathbf{C}_χ is the sum of \mathbf{C}_d , the data covariance matrix, and \mathbf{C}_p , the matrix of prediction un-
 349 certainties accounting for uncertainties in the elastic structure (see Rousset et al., 2016,
 350 for a description of how we build \mathbf{C}_p). We build the data covariance matrix assuming
 351 different datasets (i.e. InSAR and GNSS velocities) are independent. We evaluate the
 352 covariance of the InSAR velocity maps over regions with no identified deformation sig-
 353 nals (e.g. Sudhaus & Jónsson, 2009; Jolivet, Simons, et al., 2015, and supp. mat. Fig.
 354 S-30). Effectively, since we retain InSAR data less than 60 km away from the fault, we
 355 expect InSAR data to constrain mostly the distribution of shallow slip while far field GNSS
 356 velocities should constrain the deep slip rate.

357 Since we use bounded uniform and Gaussian prior PDFs, there is no analytical for-
 358 mulation of the model that best fits the data, although a bounded normal distribution
 359 is expected (Nocquet, 2018b). We use AlTar, a stochastic sampler using elements of par-
 360 allel tempering, to draw 90,000 samples from the posterior PDF ([https://github.com/
 361 AlTarFramework/altar](https://github.com/AlTarFramework/altar); Minson et al., 2013; Jolivet, Simons, et al., 2015). Doing so,
 362 we explore the range of models that explain the data without the use of any form of reg-
 363 ularization (i.e. smoothing) apart from the choice of the geometry of the fault (i.e. as
 364 opposed to trans-dimensional methods, Dettmer et al., 2014). AlTar uses parallel tem-
 365 pering to let the sample set slowly converge toward the posterior PDF. Here, we need
 366 62 iterations to let the 90,000 Markov chains converge (see Fig. S-28 for an example of
 367 convergence for the marginal of the deep slip rate on the NAF).

368 In figure 3, we show the mean of the 90,000 samples and the corresponding stan-
 369 dard deviation. First, we see that the slip rate on deep dislocations is 20 ± 0.6 mm/yr,
 370 consistent with the expected relative pate motion rate at this location. Second, we ob-

371 serve that, given the large size (> 5 km) of triangles of the fault mesh at the bottom
 372 end of the shallow section of the NAF, locking depth can be effectively anywhere between
 373 15 and 20 km everywhere along the fault, except where surface aseismic slip is observed.
 374 Third, below the 60-70 km long segment that slips rapidly at the surface between Ismet-
 375 pasa and Bayramoren, we observe a shallower locking depth between 8 and 12 km. Along
 376 this segment, slip rates locally reach 20 ± 3 mm/yr with potentially two distinct slip patches.
 377 In addition, along this same section, we observe a locked section at depth from roughly
 378 5 to 10 km-depth. Near the city of Ismetpasa, we observe a patch of dip slip with slip
 379 rates as high as 12 ± 3 mm/yr, although this patch is very limited in size. Other along
 380 strike variations of slip rate are not significant compared to the standard deviation and
 381 correspond to areas where InSAR decoherence led to poor surface velocity reconstruc-
 382 tion. Figures S-24, S-26 and S-31 to S-34 of the supplementary informations show how
 383 the mean model performs at fitting the data. Note that the mean model does not be-
 384 long to the ensemble of models drawn from the posterior PDF and is expected to show
 385 lower performance than models actually within our sample set. Since the posterior PDF
 386 is expected to be a multivariate bounded Gaussian distribution, the mean model should
 387 not be too different from the best fit model.

388 As a conclusion, the distribution of slip rates along the NAF in the region of Is-
 389 metpasa can be summarized as (1) a rapidly slipping segment east of Ismetpasa extend-
 390 ing over 60-70 km with slip rates as high as 20 mm/yr, (2) a shallow locking depth be-
 391 tween 8 and 12 km-depth below the segment of Ismetpasa and (3) a locking depth be-
 392 tween 15 and 20 km-depth elsewhere (Fig. 3).

393 5 Time-dependent surface slip

394 We explore time-dependent surface slip as directly measured in the InSAR time
 395 series. We apply a similar approach to Dalaison et al. (2021) to extract shallow slip along
 396 the NAF from the time series of LOS displacements. We first extract, 500 m-wide, fault
 397 perpendicular profiles of LOS displacements every 250 m along the NAF at each acqui-
 398 sition time of each of the three time series on tracks 65, 87 and 167. We then extract the
 399 across fault step in LOS displacement and interpolate these values in time and space to
 400 combine them into time series of strike slip (i.e. fault parallel slip component) and dip
 401 slip (i.e. across fault vertical differential motion).

402 We show in Figure 4 the space and time evolution of surface slip along the section
 403 where aseismic slip has been identified in previous studies. In addition, we apply the deep
 404 denoiser developed by Rouet-Leduc et al. (2021) in order to detect the most important
 405 variations of surface slip. This denoiser is a trained convolutional neural network specif-
 406 ically designed to remove tropospheric artefacts from time series of LOS apparent dis-
 407 placements. Effectively, the denoiser removes what is identified as noise (i.e. here Gaus-
 408 sian correlated noise, topography correlated phase values and isolated pixels showing anoma-
 409 lous values wrt. their surrounding pixels) and highlights surface displacement consistent
 410 with those produced by dislocations embedded in an elastic halfspace. Moreover, this
 411 procedure reveals signals that are consistently growing with time, unlike tropospheric
 412 artefacts. Here, we show the instantaneous slip rate as measured on the output of the
 413 denoiser, considering the time spanned by the acquisitions used as input to the neural
 414 network. Finally, these results are compared with ground-truth measurements from a
 415 local creepmeter (Bilham et al., 2016). In supplementary informations figures S-19 and
 416 S-21, we show the uncertainties associated with the strike slip estimates and the verti-
 417 cal differential motion across the fault.

418 The history of strike slip along the aseismic section extending east of Ismetpasa shows
 419 along strike variations. We observe slip rate accelerations and decelerations over a 30 km-
 420 long section of the NAF, extending from 10 km west (Lon 32.5°) to 20 km east (Lon 32.85°)
 421 of Ismetpasa. Surface slip events lasting a few days to a few weeks can be seen, for in-
 422 stance from +10 km to +20km from Ismetpasa early 2016 in Figure 4. Some of these
 423 slip events are also captured by the creepmeter in Ismetpasa, such as the ~ 5 mm slip
 424 events in mid-2017 and late 2020 (Fig. 4). These events are visible in the surface slip
 425 evolution in Figure 4 at Ismetpasa (km 0). The denoiser detect these two transients, which
 426 display similar along-strike length as the event detected in 2013 by Rousset et al. (2016)
 427 and cleaned up by Rouet-Leduc et al. (2021). Their spatial extent is directly visible in
 428 the time series (Fig. S-22 of supplementary materials) although it does not stand out
 429 clearly enough from the noise to allow us to model their depth extent. The correspond-
 430 ing denoised surface displacements is not helpful to constrain the depth extent as the
 431 neural network is yet unable to recover the long wavelength of a deformation field (Rouet-
 432 Leduc et al., 2021).

433 Interestingly, we do not observe transient slip accelerations over the easternmost
 434 section. From 20 to 75 km east of Ismetpasa, we record steady surface slip with no ob-

435 various slow slip events. The denoiser also does not capture sudden slip accelerations, sug-
 436 gesting that slow slip events are not hidden in the noise of our time series. If occurring,
 437 slow slip events may be too small to be recorded by InSAR. More sensitive, local instru-
 438 ments such as creep- or strain-meters should be installed.

439 Vertical differential motion across the fault observed in the westernmost section also
 440 does not show sudden accelerations (Fig. S-21). Potential periodic signals in the verti-
 441 cal differential motion can be seen in the central section between +20 km and +30 km,
 442 although the corresponding variations are small (i.e. less than 4 mm) hence should be
 443 taken with caution. No significant differential vertical motion is observed east of +40 km
 444 of the section.

445 **6 Discussion**

446 As a summary, the central section of the North Anatolian Fault can be character-
 447 ized by the presence of a 60 km-long section that slips continuously since, at least the
 448 1980's (Altay & Sav, 1991). Since no significant seismicity is observed along the section
 449 at least since the 60's, slip is considered to be mostly aseismic. Slow slip events are ob-
 450 served every 2.5 years with 5 to 15 mm of slip at the surface over the westernmost part
 451 of the aseismic segment. The eastern part of the segment slips continuously at rates reach-
 452 ing 1 cm/yr, half of the relative plate motion expected at this location. At depth, aseis-
 453 mic slip extends from the surface to a depth of 5 to 6 km. Below, the fault is locked over
 454 a 4 to 5 km-wide portion. The locking depth below this aseismic section is relatively shal-
 455 low, 12 km, compared to the 15 to 20 km observed elsewhere along the fault where no
 456 surface aseismic slip is observed.

457 **6.1 Consistency of creepmeter and InSAR measurements**

458 The first notable element of discussion is the accuracy and precision of both InSAR
 459 data and creepmeter measurements. Creepmeters installed in Ismetpasa measure rela-
 460 tive displacement over a 20 m (Altay & Sav, 1991) or 16.6 m (Bilham et al., 2016) dis-
 461 tance with a 30° angle with respect to the local orientation of the NAF (Altay & Sav,
 462 1991; Bilham et al., 2016). One could argue that these instruments would measure very
 463 local fault slip, spanning a very shallow depth along dip. Our InSAR data show that both
 464 slow slip averaged over several years of measurements and the slow slip events captured

465 by the creepmeters actually extend for several kilometers along strike. The 2013 slow
 466 slip event, even though not captured by creepmeters as no instrument was installed at
 467 the time, is 5-8 km-long and extends down to 4 km at depth Rousset et al. (2016). Events
 468 captured by our time series of InSAR data are of comparable along-strike extent and slip.
 469 Furthermore, InSAR time series have 120 m-sized pixels and we evaluate surface slip by
 470 linear regression of the InSAR data over several kilometers on both sides of the fault.
 471 Therefore, the slow slip events captured by our InSAR time series are probably span-
 472 ning the first kilometers at depth, although our data is too noisy to allow accurate slip
 473 modeling. This means that the largest events captured by creepmeters are indeed span-
 474 ning several kilometers at depth, a depth much larger than the creepmeter baseline length
 475 would lead to consider. Such consistency between different measurement methods also
 476 leads to conclude that, to first order, there is no significant variations in slip at depth
 477 during the slow slip events at Isetmpasa between the surface and a depth of 1 to 2 km.

478 We note that slip events captured by the creepmeter prior to 2016 are neither vis-
 479 ible in our InSAR time series, although a slight long term trend is visible, nor detected
 480 by our neural network (Fig. 4). These events could be local and affect a section of the
 481 fault too small to be detected by InSAR. During the 2014-2016 period, only one Sentinel
 482 1 satellite (Sentinel 1-A) was operational and the frequency of SAR acquisitions only dou-
 483 bled with the launched of Sentinel 1-B. The lower sensitivity to mm-to-cm slip events
 484 during the 2014-2016 could also be related to such lower rate of repetition of acquisitions.

485 **6.2 time-dependent slow slip and the rheology of the aseismic section**

486 Comparing results with previously published ones, the along strike distribution of
 487 surface slip rates we infer is comparable to that measured by Cetin et al. (2014) and Kaneko
 488 et al. (2012) with Envisat data over the 2003-2010 period. We observe a gradual increase
 489 in slip rates east of Isetmpasa, reaching up to 1 cm/yr, and a decrease further east over
 490 the 60 km-long segment. The only notable exception is a 10 km-long fast slipping sec-
 491 tion observed by Cetin et al. (2014) in the 2003-2010 data with rates as high as 2 cm/yr,
 492 20 to 30 km east of Isetmpasa. Such high rates have not been described by Kaneko et
 493 al. (2012) with the same data. In addition, we observe that, over the 2014-2020 period,
 494 slip rates to the east of Isetmpasa are remarkably stable with no significant temporal vari-
 495 ations. As no ground-based measurements are available for that part of the fault, we have
 496 to compare InSAR measurements inferred from data acquired by different satellites and

497 processed with different techniques. For instance, Cetin et al. (2014) used a persistent
 498 scatterer method to process the data and obtained fewer pixels compared to our SBAS-
 499 like approach but with a potentially higher precision in the velocity measurement. Al-
 500 though it would be tempting to conclude on a local drop in velocity from 2 to 1 cm/yr
 501 in the central part of the section between the periods covered by Envisat data (2001-2010)
 502 and by Sentinel 1 data (2014 onwards), we prefer to remain cautious on this point be-
 503 cause of the inconsistency between measurements by Cetin et al. (2014) and Kaneko et
 504 al. (2012). The relative temporal stability of surface slip over the 2014-2020 period ac-
 505 tually advocates for a stable slip rate over the last 2 decades.

506 Near Ismetpasa, early creepmeter measurements revealed the occurrence of slow slip
 507 events in the 1980's (Altay & Sav, 1991). Comparable accelerations are described by Rousset
 508 et al. (2016) and Bilham et al. (2016) in 2013 and 2014-2016. As rightly pointed out by
 509 Bilham et al. (2016), aliasing of measurements with different and potentially uneven tem-
 510 poral sampling leads to different conclusions. That said, over periods of several days, rates
 511 vary by one to two orders of magnitude as shown in figure 5. Averaging over years of mea-
 512 surements, the slip rate at Ismetpasa is, to the contrary, remarkably stable, although a
 513 slight decay may be considered (Fig. 5). After a revisit of the measurement of the origi-
 514 nal wall offset by Ambraseys (1970), Bilham et al. (2016) proposed a corrected estimate
 515 of the surface slip rate in the 1960's of 1 cm/yr. In addition, Bilham et al. (2016) dis-
 516 cards the early measurement of an offset in railroad tracks as deemed too uncertain, in
 517 agreement with the original report by Ambraseys (1970). Using the corrected slip rates
 518 from Bilham et al. (2016), one may consider a decrease in averaged slip rates (Fig. 4),
 519 from 1 cm/yr in 1970 to 6 ± 2 mm/yr in 2020. A bayesian linear regression through the
 520 velocity estimates suggests a deceleration of 0.07 ± 0.01 mm/yr² from 1960 to 2020. How-
 521 ever, the uncertainty provided with the measurement on the wall photograph from 1969
 522 is 0.4 mm/yr, a value probably too small for such measurement. Similar concern may
 523 be raised for other measurements with uncertainties lower than one mm/yr based on his-
 524 torical photographs. Considering uncertainties might have been underestimated, the de-
 525 crease in slip rate at Ismetpasa is not statistically significant anymore.

526 Therefore, since the slip rate estimate inferred by Ambraseys (1970) for the 1944-
 527 1950 time period has been discarded by Bilham et al. (2016) as too uncertain, the hy-
 528 pothesis of a long standing post-seismic decay put forward by Kaneko et al. (2012) and
 529 Cetin et al. (2014) becomes difficult to accept. The expected logarithmic decay of slip

530 rates following a large earthquake is not shown by the data as only a slight decrease in
531 slip rates is visible from 1960 to today. We cannot discard the hypothesis that afterslip
532 occurred after the 1944 earthquake, as would be expected for such a large earthquake,
533 but we simply cannot reject nor support this hypothesis with the available data. Con-
534 ditions for such post-seismic afterslip are the presence of a locked, seismogenic asperity
535 at depth, as confirmed by our and previously published analysis (e.g. Cetin et al., 2014;
536 Bilham et al., 2016), and the presence of rate-strengthening material near the surface.
537 The depth-dependence of constitutive parameters of friction laws suggests that rate-strengthening
538 material is to be expected near the surface (e.g. Blanpied et al., 1991; Scholz, 1998), but
539 is not confirmed by geodetic data here as no obvious post-seismic signal is observed.

540 If constitutive properties of the fault were to explain the occurrence of aseismic slip
541 along this section, then it would also require along strike rheological variations in addi-
542 tion to the expected depth-dependency. Rocks exposed at the surface along the aseis-
543 mic segment include volcanic deposits, sedimentary units (limestones) and metamorphic
544 rocks (Cetin et al., 2014), suggesting no specific link between rock type and slip behav-
545 ior. Kaduri et al. (2019) propose a relationship between the development of a specific
546 mineralogical fabric in the fault material and the occurrence of aseismic slip, suggest-
547 ing that the peculiar slip behavior of this segment, compared to the rest of the NAF that
548 ruptured during the 1944 and 1943 earthquakes, may be related to the occurrence of pres-
549 sure solution creep in the fault gouge. Similar observations have been made along the
550 Longitudinal Valley fault in Taiwan and the San Andreas Fault in California (Thomas
551 et al., 2014; Gratier et al., 2011). The question that then remains is why would such a
552 segment develop along this particular segment of the NAF and not elsewhere.

553 Finally, it is important to realize that all reports of aseismic slip published to date
554 focused on the surroundings of the city of Ismetpasa, with the exception of Cetin et al.
555 (2014) and Kaneko et al. (2012). At this peculiar location, as pointed out earlier by Aytun
556 (1982), we observe vertical differential motion across the fault, consistent with subsidence
557 measured north of the fault near Ismetpasa. Such subsidence is probably related to hy-
558 drological effects. Furthermore, this specific section is the only section where we observe
559 slow slip events. Therefore, the slip behavior of the NAF in Ismetpasa is not represen-
560 tative of that of the entire creeping section.

561 All in all, it is difficult to conclude firmly on the rheology of fault material along
 562 this aseismic section. Aseismic slip seems steady, or slightly decaying, since at least the
 563 1960's to the exception of the peculiar location of Ismetpasa. If further evidence of post-
 564 seismic slip following the 1944 earthquake were to be put forward, then an effective rate-
 565 strengthening rheology should be considered. In such case, slow slip events in Ismetpasa
 566 can be explained by the presence of small heterogeneities in frictional constitutive prop-
 567 erties (Wei et al., 2013). Without any additional evidence, fault rheology is still a mat-
 568 ter of debate as aseismic slip may result from a large nucleation size, geometrical com-
 569 plexities or low normal stress conditions. For instance, in the case of rate-weakening prop-
 570 erties, reduced normal stress results in a large nucleation size hence promotes slow slip
 571 and spontaneous slow slip events may occur at the transition between locked and creep-
 572 ing regions (e.g. Liu & Rice, 2005).

573 **6.3 A simple, testable explanation for shallow aseismic slip**

574 Although the lack of evidence to constrain the rheology of fault material in this re-
 575 gion might be disappointing, the geometry of the distribution of aseismic slip at depth
 576 may provide an explanation for the occurrence of shallow slip in this region. As shown
 577 by our model, the locking depth below the aseismic slip segment is shallower than else-
 578 where along the fault (Fig. 3). Such shallow locking depth is actually the only feature
 579 that differentiates the creeping segment from the rest of the fault covered by our study.
 580 This particular slip distribution is highlighted by the characteristic pattern of surface
 581 displacement rates, showing a gradual change in velocity approaching the fault (Fig. S-
 582 16 of supplementary materials). This bending, visible between 10 km away from the fault
 583 and the fault trace, is interpreted as the signature of elastic stress building up on a locked
 584 asperity. Since the fault slips at the surface, as highlighted by the step-like change in sur-
 585 face velocity across the fault, this locked asperity must be located between the locking
 586 depth and the bottom of the creeping zone.

587 Shallow locking depth results in higher stressing rates at the surface. For a semi-
 588 infinite dislocation embedded in an elastic halfspace buried at a depth d , shear stress-
 589 ing rate, $\dot{\tau}$, at the surface writes as $\dot{\tau} = \frac{\mu\dot{\delta}}{2\pi d}$ with μ the shear modulus and $\dot{\delta}$ the slip
 590 rate on the fault. Assuming a constant shear modulus and slip rates, shallowing the lock-
 591 ing depth d from 20 to 10 km results in a twofold increase in stressing rate. For instance,
 592 with a 2 cm/yr slip rate and a 30 GPa shear modulus, shear stressing rate at the sur-

593 face jumps from approximately 5 to 10 kPa/yr. Alone, such change in shear stressing
594 rate should not lead to any change in slip behavior.

595 Whether shallow fault material is rate-weakening or -strengthening, the depth-distribution
596 of effective normal stress, the difference between normal stress and pore pressure, influ-
597 ences frictional resistance. Low normal stress implies slip occurs at lower shear stress for
598 a given coefficient of friction. Then, if shallow fault material is rate-strengthening, a higher
599 (resp. lower) shear stressing rate should lead to the occurrence of constant shallow slow
600 slip earlier (resp. later) in between two large earthquakes. If shallow fault material is rate-
601 weakening, we must consider the depth-distribution of nucleation size.

602 Nucleation size is inversely proportional to normal stress (e.g. Ampuero & Rubin,
603 2008) and large nucleation size leads to conditionally stable slip. If the nucleation size
604 is larger than the size of the fault, then slip cannot become dynamic and slip rates will
605 remain slow. Effective normal stress results from the combination of overburden and pore
606 pressure. To first order, normal stress increases linearly with depth, controlled by the
607 density of crustal rocks. Considering the evolution of permeability with normal stress,
608 it can be shown that effective normal stress increases with overburden until a depth of
609 3 to 5 km, depth below which normal stress is constant (Rice, 1992). There is therefore
610 a lowering of normal stress at the surface and the depth distribution of normal stress re-
611 sults in a variation in nucleation size inversely proportional to depth, with maximum nu-
612 cleation size at the surface. Considering such depth distribution of nucleation size is con-
613 stant along strike, a local shallowing of the locking depth resulting in an increase in shear
614 stressing rate at the surface would potentially increase slip rate at the surface while keep-
615 ing slip to sub-dynamic speed (i.e. slow).

616 In both rate-strengthening or -weakening shallow fault material, a shallow (resp.
617 deep) locking depth may result in faster (resp. slower) surface slip rates. In particular,
618 such hypothesis does not involve any along strike variations of rheology or fluid content
619 as only the shallowing of the locking depth is involved. Under these conditions, a homo-
620 geneous along strike fault rheology would be sufficient to explain spatial and temporal
621 variations in surface aseismic slip rates. This hypothesis should now be evaluated care-
622 fully as other parameters may play a role, such as the constitutive parameters or the evo-
623 lution of stresses in between two large earthquakes. Obviously, a physical explanation
624 to a local variation in locking depth is unfortunately missing.

625 7 Conclusion

626 We provide 100 m-scale resolution time series of surface displacement across the
 627 North Anatolian Fault from Sentinel 1 InSAR data in order to explore the details of the
 628 spatial and temporal distribution of aseismic slip along the creeping section of Ismetpasa.
 629 We confirm the presence of aseismic slip over the shallow portion of the fault (surface
 630 to 5 km-depth), collocated with a shallow locking depth (10-12 km-depth). Our surface
 631 displacement data is elsewhere compatible with a 15-20 km locking depth. Current con-
 632 clusions suggest that the evidence put forward to support the notion of long lasting af-
 633 terslip following the 1944 earthquake are subject to debate, which, unfortunately, does
 634 not allow to conclude firmly on the rheology of the fault at shallow depth. Although our
 635 data cannot exclude a generic depth-dependent behavior of the relationship between slip
 636 rate and friction, the occurrence of slow slip events and the variability of rocks exposed
 637 at the surface forces to consider that rock type, hence constitutive properties, might not
 638 be the primary control on the presence of aseismic slip along this fault segment. Oth-
 639 erwise, one would need to consider the occurrence of shallow slow slip all along the fault,
 640 where large, $M_w > 7$ earthquakes have occurred over the 20th century and not only near
 641 Ismetpasa. We propose that shallow locking depth plays a role, although further inves-
 642 tigation is needed to explain such particular feature.

643 Acknowledgments

644 The authors would like to thank Dr Harsha S. Bhat, Dr Cécile Lasserre, Pr. Pierre Dublanchet
 645 and Pr. Dmitry Garagash for insightful discussions. This project has received funding
 646 from the European Research Council (ERC) under the European Union’s Horizon 2020
 647 research and innovation program (Grant Agreements 758210 for project Geo4D). Romain
 648 Jolivet acknowledges funding from the Institut Universitaire de France. We thank the
 649 European Space Agency for the acquisition and the distribution of the SAR data by the
 650 Sentinel 1 constellation (may it fly forever and ever). InSAR data are available for down-
 651 load here: <https://peps.cnes.fr/>. ERA-Interim products are directly available for down-
 652 load at ECMWF (<https://www.ecmwf.int/>). InSAR data have been processed using
 653 the ISCE framework (<https://github.com/isce-framework/isce2>). Creepmeter data
 654 have been downloaded at the Unavco repository for geodetic data ([https://www.unavco](https://www.unavco.org/data/strain-seismic/creep-data/creep-data.html)
 655 [.org/data/strain-seismic/creep-data/creep-data.html](https://www.unavco.org/data/strain-seismic/creep-data/creep-data.html)). IGS data are available
 656 here <http://www.igs.org>. GNSS data from the Turkish national network are available

657 here: <https://www.tusaga-aktif.gov.tr/>. Data collected in the field with out sta-
658 tions along the North Anatolian Fault have been uploaded at <http://osf.io/9t3n7>.
659 Modeling has been conducted using elements of the Classic Slip Inversion library ([https://](https://github.com/jolivet/csi)
660 github.com/jolivet/csi) and AlTar (<https://github.com/AlTarFramework/altar>).
661 Notebooks detailing the procedure will be made available on Romain Jolivet's personal
662 webpage.

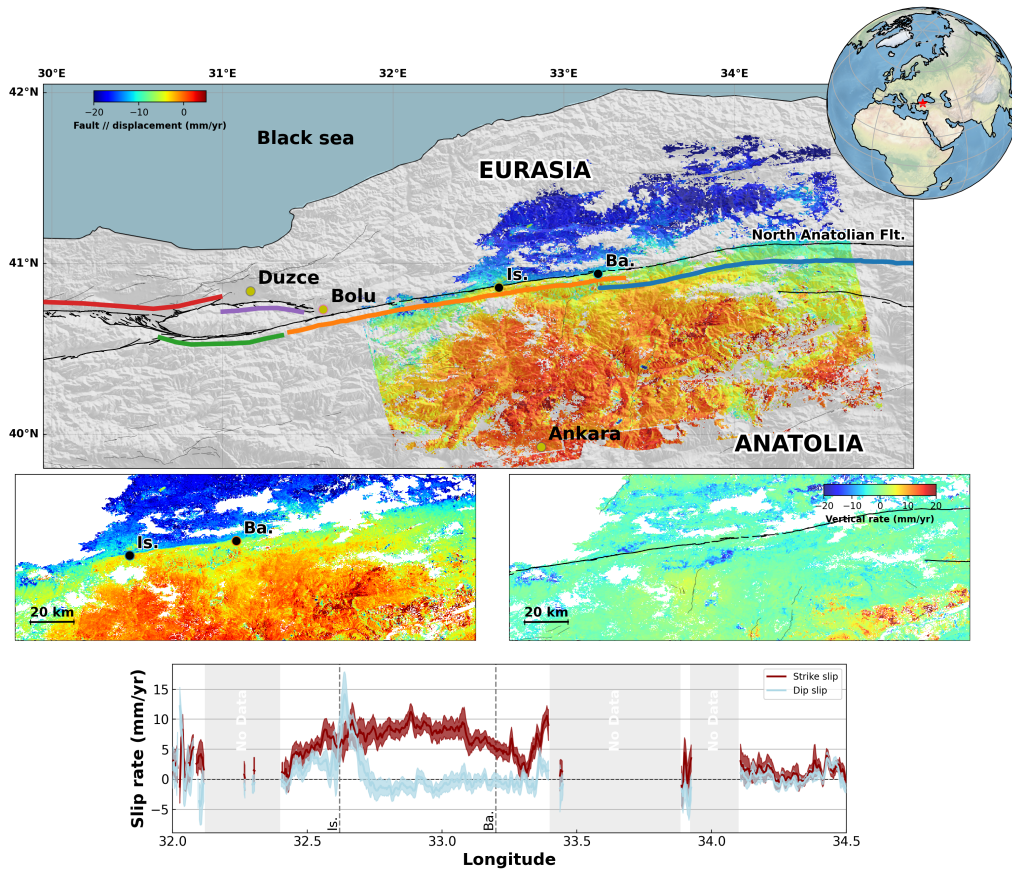


Figure 1. Fault parallel velocity map, vertical velocity map and surface slip - Top panel: Color indicates the fault parallel velocity derived from the combination of LOS velocity maps on Sentinel 1 ascending and descending tracks. Dark lines indicate the main trace of the North Anatolian Fault. Grey lines are secondary faults. Colored lines indicate the along strike extent of large historical and recent earthquakes including the 1943 M_w 7.6 Tosia-Ladik earthquake (blue), the 1944 M_w 7.3 Bolu-Gerede earthquake (orange), the 1967 M_w 7.2 Mudurnu earthquake (green), the 1999 M_w 7.6 Izmit earthquake (red) and the 1999 M_w 7.2 Düzce earthquake (purple). Center-left panel is a zoom on the area where aseismic slip is most visible, extending over the entire creeping section. Center-right panel shows the vertical displacement rate over that same area (positive is uplift). Lower panel shows surface slip rate along the fault as measured on the InSAR velocity maps. Red is strike slip while light blue is dip slip (i.e. effectively differential vertical motion at the fault trace). Grey shading shows areas of low coherence and data is missing. On all panels, Is. and Ba. indicate the location of the cities of Ismetpasa and Bayramoren, located at the end-points of the segment that slips aseismically.

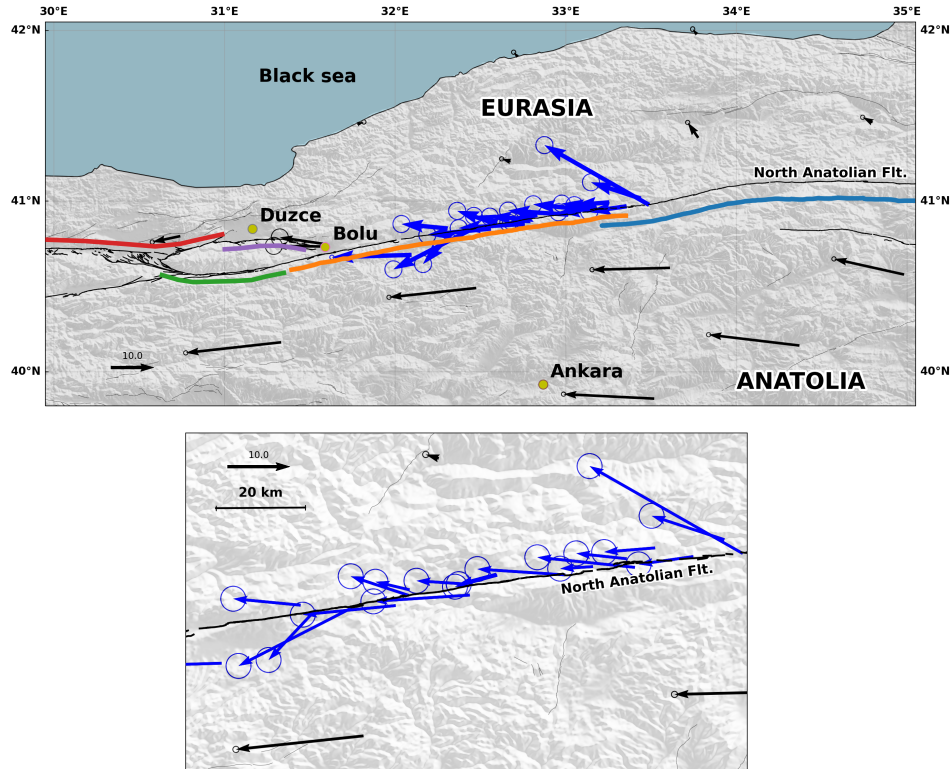


Figure 2. GNSS-derived velocities - Map of the GNSS-derived velocities from sites from the Turkish national network (in black) and from the Ismenet experiment (blue). A detailed description of the site setup for the Ismenet experiment as well as details of the data processing can be found in the supplementary information. Dark lines indicate the main North Anatolian fault. Gray lines are secondary faults. Colored lines indicate the along strike extent of large historical and recent earthquakes including the 1943 M_w 7.6 Tosia-Ladik earthquake (blue), the 1944 M_w 7.3 Bolu-Gerede earthquake (orange), the 1967 M_w 7.2 Mudurnu earthquake (green), the 1999 M_w 7.6 Izmit earthquake (red) and the 1999 M_w 7.2 Düzce earthquake (purple). Bottom panel is a close up on the region where aseismic slip has been identified. We see a clear change in measured velocities across the North Anatolian fault.

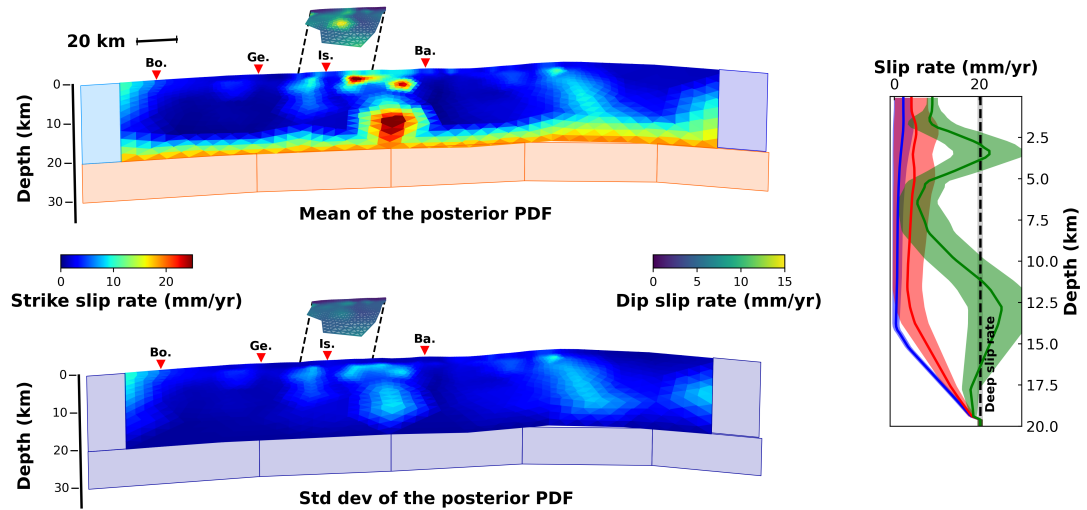


Figure 3. Fault slip distribution and uncertainties - Top: Mean of the posterior Probability Density Function of slip rate (strike slip). Rectangles on the side represent the dislocations used to model the western and eastern extension of the fault model as well as the deep dislocation modeling the far field displacement rate. Note that these dislocations extend sideways and at depth as semi-infinite structures. Small fault structure offset from the main fault shows the distribution of dip slip rate in the vicinity of the subsiding basin north of the city of Ismetpasa. Red triangles are cities located along the fault, including Bolu (Bo.), Gerede (Ge.), Ismetpasa (Is.) and Bayramoren (Ba.). **Bottom:** Standard deviation of the slip rate (strike slip and dip slip) posterior PDF. **Right:** Depth distribution of slip rate with associated uncertainties at longitude 31.9°E (blue), 32.9°E (green) and 33.9°E (red). Longitude 32.9°E is within the creeping section. Dark dashed line is the deep slip rate. The effective locking depth within the creeping section is inferred somewhere between 10 and 12.5 km depth.

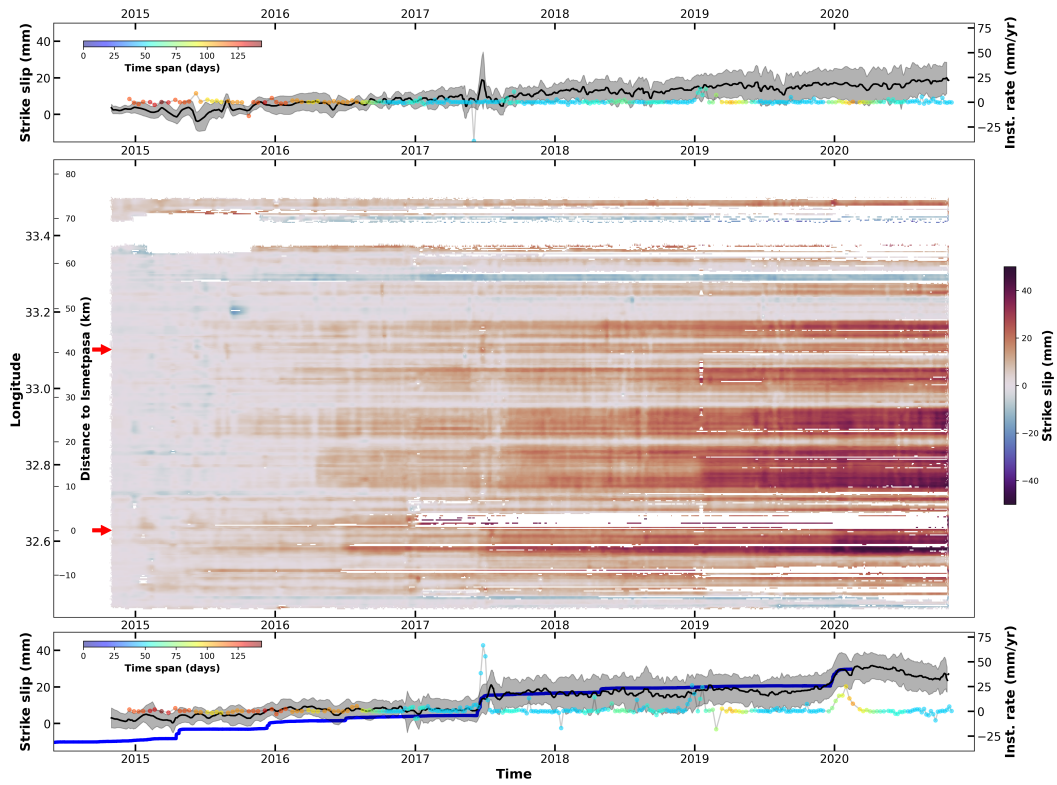


Figure 4. Time dependent surface slip rate - Space and time dependent surface slip rate (strike slip) obtained from regularly spaced profiles (see supp. mat.) Y-axis is labeled as a function on longitude and distance to Ismetpassa. Top and bottom plots show the time evolution of surface slip (dark) with the associated uncertainties (gray shading) at two distinct locations, including the Ismetpassa train station (bottom) and at 33.1°N (top). Both locations are indicated by red arrows on the main plot. Colored dots indicate the slip rate measured on sets of 9 consecutive acquisitions cleaned from atmospheric noise with a convolutional neural net (Rouet-Leduc et al., 2021). Color indicates the time span of the 9 acquisitions. Blue line is the strike slip measured by the creepmeter installed at the Ismetpassa train station Bilham et al. (2016).

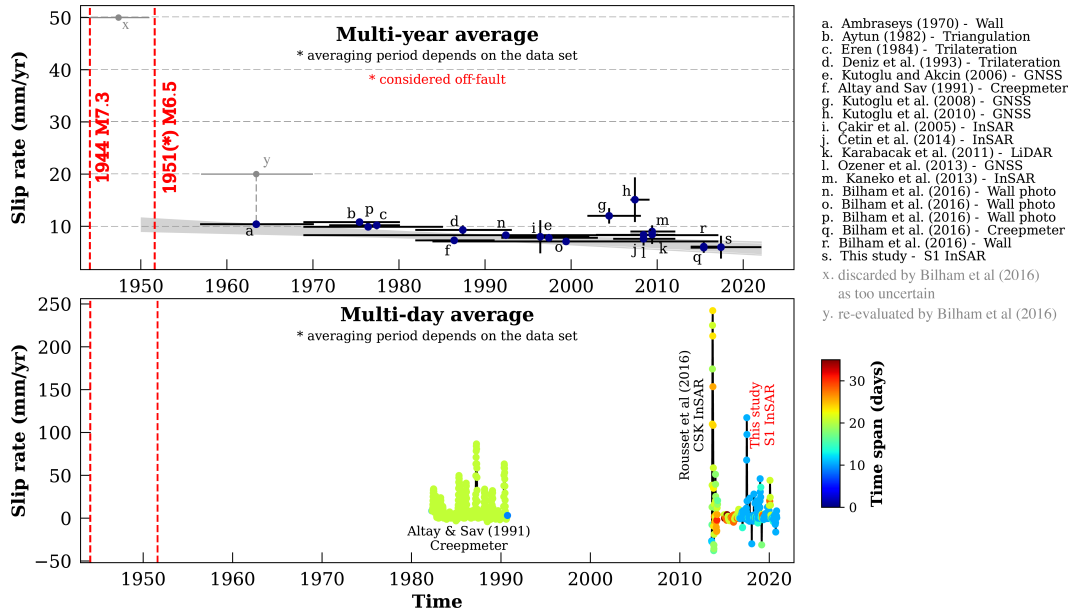


Figure 5. Evolution of surface aseismic slip rate at Isetmpasa - Surface slip rates averaged over several years (top) and over variable but day-to-week time scales (bottom). Colored dots indicate the time span over which slip rate has been estimated. Red dashed lines indicate the time of occurrence of the 1944 M_w 7.3 Bolu-Gerede and the 1951 M_w 6.5 Isetmpasa earthquakes. Gray shading indicates the range of possible models allowed from a Bayesian linear regression through the velocity estimates. Data are from Ambraseys (1970), Aytun (1982), Eren (1984), Deniz et al. (1993), Altay and Sav (1991), Çakir et al. (2005), Kutoglu and Akcin (2006), Kutoglu et al. (2008), Kutoglu et al. (2010), Karabacak et al. (2011), Deguchi (2011), Ozener et al. (2013) and Kaneko et al. (2012). Some rates were re-evaluated by Bilham et al. (2016). A table with the slip rates can be found in the supplementary informations.

663 **References**

- 664 Agram, P. S., Jolivet, R., Riel, B., Lin, Y. N., Simons, M., Hetland, E., . . . Lasserre,
 665 C. (2013). New Radar Interferometric Time Series Analysis Toolbox Released.
 666 *Eos*, *94*(7), 69–76. doi: 10.1029/2011JB008731
- 667 Altamimi, Z., Rebischung, P., Métivier, L., & Collilieux, X. (2016). ITRF2014: A
 668 new release of the International Terrestrial Reference Frame modeling nonlin-
 669 ear station motions. *Journal of Geophysical Research: Solid Earth*, *121*(8),
 670 6109–6131. doi: 10.1002/2016JB013098
- 671 Altay, C., & Sav, H. (1991). Continuous creep measurement along the North Anato-
 672 lian Fault zone. *Bulletin of the geological congres of Turkey*, *6*, 77–84.
- 673 Ambraseys, N. N. (1970). Some characteristic features of the Anatolian fault zone.
 674 *Tectonophysics*, *9*, 143–165.
- 675 Ampuero, J.-P., & Rubin, A. M. (2008). Earthquake nucleation on rate and state
 676 faults – Aging and slip laws. *Journal of Geophysical Research*, *113*(B1),
 677 B01302–21. doi: 10.1029/2007JB005082
- 678 Avouac, J.-P. (2015). From Geodetic Imaging of Seismic and Aseismic Fault Slip
 679 to Dynamic Modeling of the Seismic Cycle. *Annual Review of Earth and Plan-
 680 etary Sciences*, *43*(1), 233–271. doi: 10.1146/annurev-earth-060614-105302
- 681 Aytun, A. (1982). Creep Measurements in the Ismetpaşa Region of the North
 682 Anatolian Fault Zone. *Multidisciplinary Approach to Earthquake Prediction
 683 Progress in Earthquake Prediction Research*, *2*, 279–292.
- 684 Barbot, S., & Weiss, J. R. (2021). Connecting subduction, extension, and shear
 685 localization across the aegean sea and anatolia. *Geophysical Journal Interna-
 686 tional*, *226*(1), 422–445. doi: 10.1093/gji/ggab078
- 687 Barka, A. (1996). Slip distribution along the north anatolian fault associated with
 688 the large earthquakes of the period 1939 to 1967. *Bulletin of the Seismological
 689 Society of America*, *86*(5), 1238–1254.
- 690 Benoit, A., Pinel-Puysegur, B., Jolivet, R., & Lasserre, C. (2020). CorPhU: an
 691 algorithm based on phase closure for the correction of unwrapping errors in
 692 SAR interferometry. *Geophysical Journal International*, *221*(3), 1959–1970.
 693 doi: 10.1093/gji/ggaa120
- 694 Bevis, M., & Brown, A. (2014). Trajectory models and reference frames for crustal
 695 motion geodesy. *Journal of Geodesy*, *88*(3), 283–311. doi: 10.1007/s00190-013

696 -0685-5

- 697 Bilham, R., Ozener, H., Mencin, D., Dogru, A., Ergintav, S., Çakir, Z., . . . Mattioli,
 698 G. (2016). Surface creep on the North Anatolian Fault at Ismetpasa, Turkey,
 699 1944-2016. *Journal of Geophysical Research-Solid Earth*, *121*, 7409–7431. doi:
 700 10.1002/2016JB013394
- 701 Blanpied, M. L., Lockner, D. A., & Byerlee, J. D. (1991). Fault stability inferred
 702 from granite sliding experiments at hydrothermal conditions. *Geophysical Re-*
 703 *search Letters*, *18*(4), 609–612. doi: 10.1029/91GL00469
- 704 Bletery, Q., Cavalié, O., Nocquet, J.-M., & Ragon, T. (2020). Distribution of inter-
 705 seismic coupling along the north and east anatolian faults inferred from insar
 706 and gps data. *Geophysical Research Letters*, *47*(16), e2020GL087775. doi:
 707 10.1029/2020GL087775
- 708 Bouchon, M., Karabulut, H., Aktar, M., Ozalaybey, S., Schmittbuhl, J., & Bouin,
 709 M. P. (2011). Extended Nucleation of the 1999 Mw 7.6 Izmit Earthquake.
 710 *Science*, *331*(6019), 877–880. doi: 10.1126/science.1197341
- 711 Bürgmann, R. (2018). The geophysics, geology and mechanics of slow fault slip.
 712 *Earth and Planetary Science Letters*, *495*, 112–134. doi: 10.1016/j.epsl.2018.04
 713 .062
- 714 Çakir, Z., Akoglu, A., Belabbes, S., Ergintav, S., & Meghraoui, M. (2005). Creeping
 715 along the Ismetpasa section of the North Anatolian fault (Western Turkey):
 716 Rate and extent from InSAR. *Earth and Planetary Science Letters*, *238*(1-2),
 717 225–234. doi: 10.1016/j.epsl.2005.06.044
- 718 Candela, T., Renard, F., Klinger, Y., Mair, K., Schmittbuhl, J., & Brodsky, E. E.
 719 (2012). Roughness of fault surfaces over nine decades of length scales. *Journal*
 720 *of Geophysical Research*, *117*(B8), B08409. doi: 10.1029/2011JB009041
- 721 Cattania, C., & Segall, P. (2021). Precursory slow slip and foreshocks on rough
 722 faults. *Journal of Geophysical Research: Solid Earth*, *126*(4), e2020JB020430.
 723 doi: 10.1029/2020JB020430
- 724 Cetin, E., Cakir, Z., Meghraoui, M., Ergintav, S., & Akoglu, A. M. (2014). Extent
 725 and distribution of aseismic slip on the Ismetpaşa segment of the North Anato-
 726 lian Fault (Turkey) from Persistent Scatterer InSAR. *Geochemistry Geophysics*
 727 *Geosystems*, *15*(7), 2883–2894. doi: 10.1002/2014GC005307
- 728 Dalaison, M., & Jolivet, R. (2020). A kalman filter time series analysis method for

- 729 insar. *Journal of Geophysical Research: Solid Earth*, 125(7), e2019JB019150.
730 doi: 10.1029/2019JB019150
- 731 Dalaison, M., Jolivet, R., & Le Pourhiet, L. (2023). A snapshot of the long-
732 term evolution of a distributed tectonic plate boundary [doi: 10.1126/sci-
733 adv.add7235]. *Science Advances*, 9(16), eadd7235. Retrieved from
734 <https://doi.org/10.1126/sciadv.add7235> doi: 10.1126/sciadv.add7235
- 735 Dalaison, M., Jolivet, R., van Rijsingen, E. M., & Michel, S. (2021). The interplay
736 between seismic and aseismic slip along the chaman fault illuminated by insar.
737 *Journal of Geophysical Research: Solid Earth*, 126(12), e2021JB021935. doi:
738 10.1029/2021JB021935
- 739 Deguchi. (2011). Detection of fault creep around naf by insar time series analysis
740 using palsar data. *Proc. of SPIE, SAR Image Analysis, Modeling, and Tech-
741 niques XI*, 8179. doi: 10.1117/12.898478
- 742 DeMets, C., Gordon, R. G., & Argus, D. F. (2010). Geologically current plate mo-
743 tions. *Geophysical Journal International*, 181(1), 1–80. doi: 10.1111/j.1365-
744 -246X.2009.04491.x
- 745 den Hartog, S. A. M., & Spiers, C. J. (2013). Influence of subduction zone condi-
746 tions and gouge composition on frictional slip stability of megathrust faults.
747 *Tectonophysics*, 600, 75–90. doi: 10.1016/j.tecto.2012.11.006
- 748 Deniz, R., Aksoy, A., Yalin, D., Seeger, H., Franke, P., Hirsch, O., & Bautsch,
749 P. (1993). Determination of crustal movements in turkey by terres-
750 trial geodetic methods. *Journal of Geodynamics*, 18(1), 13–22. doi:
751 10.1016/0264-3707(93)90024-Z
- 752 Dettmer, J., Benavente, R., Cummins, P. R., & Sambridge, M. (2014). Trans-
753 dimensional finite-fault inversion. *Geophysical Journal International*, 199(2),
754 735–751. doi: 10.1093/gji/ggu280
- 755 Dianala, J. D. B., Jolivet, R., Thomas, M. Y., Fukushima, Y., Parsons, B., &
756 Walker, R. (2020). The relationship between seismic and aseismic slip on the
757 philippine fault on leyte island: Bayesian modeling of fault slip and geother-
758 mal subsidence. *Journal of Geophysical Research: Solid Earth*, 125(12),
759 e2020JB020052. doi: 10.1029/2020JB020052
- 760 Dragert, H., Wang, K., & Thomas, J. S. (2001). A Silent Slip Event on the Deeper
761 Cascadia Subduction Interface. *Science*, 292(5521), 1525–1528. doi: 10.1126/

- 762 science.1060152
- 763 Duputel, Z., Agram, P. S., Simons, M., Minson, S. E., & Beck, J. L. (2014). Ac-
764 counting for prediction uncertainty when inferring subsurface fault slip. *Geo-*
765 *physical Journal International*, *197*(1), 464–482. doi: 10.1093/gji/ggt517
- 766 Duquesnoy, T., Barrier, E., Kasser, M., Aurelio, M., Gaulon, R., Punongbayan,
767 R. S., & Rangin, C. (1994). Detection of creep along the Philippine fault:
768 First results of geodetic measurements on Leyte island, central Philippine.
769 *Geophysical Research Letters*, *21*(11), 975–978. doi: 10.1029/94GL00640
- 770 Ellsworth, W. L., & Bulut, F. (2018). Nucleation of the 1999 Izmit earthquake by
771 a triggered cascade of foreshocks. *Nature Geoscience*, *84*, 1–6. doi: 10.1038/
772 s41561-018-0145-1
- 773 Eren, K. (1984). Strain analysis along the north anatolian fault by using geodetic
774 surveys. *Bulletin géodésique*, *58*(2), 137–150. doi: 10.1007/BF02520898
- 775 Fattahi, H., Agram, P., & Simons, M. (2016). A Network-Based Enhanced Spec-
776 tral Diversity Approach for TOPS Time-Series Analysis. *IEEE Transactions*
777 *on Geoscience and Remote Sensing*, *55*(2), 777–786. doi: 10.1109/TGRS.2016
778 .2614925
- 779 Goldstein, R. M., & Werner, C. L. (1998, November). Radar interferogram filtering
780 for geophysical applications. *Geophysical Research Letters*, *25*(21), 4035–4038.
- 781 Goldstein, R. M., Zebker, H. A., & Werner, C. L. (1988). Satellite radar interferome-
782 try: Two-dimensional phase unwrapping. *Radio Science*, *23*(4), 713–720.
- 783 Gratier, J. P., Richard, J., Renard, F., Mittempergher, S., Doan, M. L., Di Toro,
784 G., ... Boullier, A. M. (2011). Aseismic sliding of active faults by pressure
785 solution creep: Evidence from the San Andreas Fault Observatory at Depth.
786 *Geology*, *39*(12), 1131–1134. doi: 10.1130/G32073.1
- 787 Gurrola, E., Rosen, P., Sacco, G., Seliga, W., Zebker, H., Simons, M., & Sandwell,
788 D. (2010). Sar scientific computing environment. In *Paper presented at the*
789 *american geophysical union fall meeting, san francisco, ca.*
- 790 Herring, T. A., Floyd, M., King, R., & McClusky, S. C. (2015). Globk reference
791 manual, global kalman filter vlbi and gps analysis program, release 10.6. (Com-
792 puter software manual No. June). Cambridge, MA, USA. Retrieved from
793 <https://geoweb.mit.edu/gg>
- 794 Herring, T. A., King, R., Floyd, M., & McClusky, S. C. (2018). Introduction to

- 795 gamit/globk, release 10.7. (Computer software manual No. June). Cambridge,
796 MA, USA. Retrieved from <https://geoweb.mit.edu/gg>
- 797 Jolivet, R., Agram, P. S., Lin, N. Y., Simons, M., Doin, M.-P., Peltzer, G., & Li,
798 Z. (2014). Improving InSAR geodesy using Global Atmospheric Mod-
799 els. *Journal of Geophysical Research-Solid Earth*, *119*(3), 2324–2341. doi:
800 10.1002/2013JB010588
- 801 Jolivet, R., Candela, T., Lasserre, C., Renard, F., Klinger, Y., & Doin, M. P. (2015).
802 The Burst-Like Behavior of Aseismic Slip on a Rough Fault: The Creeping
803 Section of the Haiyuan Fault, China. *Bulletin of the Seismological Society of*
804 *America*, *105*(1), 480–488. doi: 10.1785/0120140237
- 805 Jolivet, R., & Frank, W. B. (2020). The Transient and Intermittent Nature of Slow
806 Slip. *AGU Advances*, *1*(1), e2019AV000126–8. doi: 10.1029/2019AV000126
- 807 Jolivet, R., Grandin, R., Lasserre, C., Doin, M. P., & Peltzer, G. (2011). Systematic
808 insar tropospheric phase delay corrections from global meteorological reanaly-
809 sis data. *Geophysical Research Letters*, *38*(17). doi: 10.1029/2011GL048757
- 810 Jolivet, R., Simons, M., Agram, P. S., Duputel, Z., & Shen, Z. K. (2015). Aseismic
811 slip and seismogenic coupling along the central San Andreas Fault. *Geophysical*
812 *Research Letters*, *42*(2), 297–306. doi: 10.1002/2014GL062222
- 813 Kaduri, M., Gratier, J.-P., Lasserre, C., Çakir, Z., & Renard, F. (2019). Quanti-
814 fying the partition between seismic and aseismic deformation along creeping
815 and locked sections of the north anatolian fault, turkey. *Pure and Applied*
816 *Geophysics*, *176*(3), 1293–1321. doi: 10.1007/s00024-018-2027-2
- 817 Kaneko, Y., Avouac, J.-P., & Lapusta, N. (2010). Towards inferring earthquake pat-
818 terns from geodetic observations of interseismic coupling. *Nature Geoscience*,
819 *3*(5), 363–369. doi: 10.1038/ngeo843
- 820 Kaneko, Y., Fialko, Y., Sandwell, D. T., Tong, X., & Furuya, M. (2012). Interseis-
821 mic deformation and creep along the central section of the North Anatolian
822 fault (Turkey): InSAR observations and implications for rate-and-state friction
823 properties. *Journal of Geophysical Research-Solid Earth*, *118*, 316–331. doi:
824 10.1029/2012JB009661
- 825 Karabacak, V., Altunel, E., & Cakir, Z. (2011). Monitoring aseismic surface creep
826 along the north anatolian fault (turkey) using ground-based lidar. *Earth and*
827 *Planetary Science Letters*, *304*(1), 64–70. doi: 10.1016/j.epsl.2011.01.017

- 828 Khoshmanesh, M., & Shirzaei, M. (2018). Multiscale Dynamics of Aseismic Slip on
 829 Central San Andreas Fault. *Geophysical Research Letters*, *45*(5), 2274–2282.
 830 doi: 10.1002/2018GL077017
- 831 Kodaira, S., Iidaka, T., Kato, A., Park, J.-O., Iwasaki, T., & Kaneda, Y. (2004).
 832 High pore fluid pressure may cause silent slip in the nankai trough. *Science*,
 833 *304*(5675), 1295–1298. doi: 10.1126/science.1096535
- 834 Kondo, H., Awata, Y., Emre, Ö., Doğan, A., Özalp, S., Tokay, F., ... Okumura, K.
 835 (2005). Slip distribution, fault geometry, and fault segmentation of the 1944
 836 bolu-gerede earthquake rupture, north anatolian fault, turkey. *Bulletin of the*
 837 *Seismological Society of America*, *95*(4), 1234–1249. doi: 10.1785/0120040194
- 838 Kondo, H., Özaksoy, V., & Yildirim, C. (2010). Slip history of the 1944 bolu-gerede
 839 earthquake rupture along the north anatolian fault system: Implications for
 840 recurrence behavior of multisegment earthquakes. *Journal of Geophysical*
 841 *Research: Solid Earth*, *115*(B4). doi: 10.1029/2009JB006413
- 842 Kutoglu, H. S., & Akcin, H. (2006). Determination of the 30-year creep trend on the
 843 ismetpaşa segment of the north anatolian fault using an old geodetic network.
 844 *Earth, Planets and Space*, *58*(8), 937–942. doi: 10.1186/BF03352598
- 845 Kutoglu, H. S., Akcin, H., Gundogdu, O., Gormus, K. S., & Koksal, E. (2010, 12).
 846 Relaxation on the ismetpasa segment of the north anatolian fault after the
 847 golcuk $m_w = 7.4$ and duzce $m_w = 7.2$ shocks. *Nat. Hazards Earth Syst. Sci.*,
 848 *10*(12), 2653–2657. doi: 10.5194/nhess-10-2653-2010
- 849 Kutoglu, H. S., Akcin, H., Kemaldere, H., & Gormus, K. S. (2008, 12). Triggered
 850 creep rate on the ismetpasa segment of the north anatolian fault. *Nat. Hazards*
 851 *Earth Syst. Sci.*, *8*(6), 1369–1373. doi: 10.5194/nhess-8-1369-2008
- 852 Liu, Y., & Rice, J. R. (2005). Aseismic slip transients emerge spontaneously in
 853 three-dimensional rate and state modeling of subduction earthquake sequences.
 854 *Journal of Geophysical Research: Solid Earth (1978–2012)*, *110*(B8), 609–14.
 855 doi: 10.1029/2004JB003424
- 856 Lohman, R. B., & Simons, M. (2005). Some thoughts on the use of InSAR
 857 data to constrain models of surface deformation: Noise structure and data
 858 downsampling. *Geochemistry, Geophysics, Geosystem*, *6*(1), Q01007. doi:
 859 10.1029/2004GC000841
- 860 Maurer, J., & Johnson, K. (2014). Fault coupling and potential for earthquakes on

- 861 the creeping section of the central San Andreas Fault. *Journal of Geophysical*
862 *Research*, 119(5), 2013JB010741–4428. doi: 10.1002/2013JB010741
- 863 Mazzotti, S., Le Pichon, X., Henry, P., & Miyazaki, S.-I. (2000). Full interseismic
864 locking of the Nankai and Japan-west Kurile subduction zones: An analysis
865 of uniform elastic strain accumulation in Japan constrained by permanent
866 GPS. *Journal of Geophysical Research: Solid Earth (1978–2012)*, 105(B6),
867 13159–13177. doi: 10.1029/2000JB900060
- 868 Minson, S. E., Simons, M., & Beck, J. L. (2013). Bayesian inversion for finite fault
869 earthquake source models I—theory and algorithm. *Geophysical Journal Inter-*
870 *national*, 194(3), 1701–1726. doi: 10.1093/gji/ggt180
- 871 Mogi, K. (1958). Relations between the Eruptions of Various Volcanoes and the De-
872 formation of the Ground Surface around them. *Bulleting of the Earthquake Re-*
873 *search Institute*, 36, 99–134.
- 874 Moreno, M., Haberland, C., Oncken, O., Rietbrock, A., Angiboust, S., & Heidbach,
875 O. (2014). Locking of the Chile subduction zone controlled by fluid pres-
876 sure before the 2010 earthquake. *Nature Geoscience*, 7(4), 292–296. doi:
877 10.1038/ngeo2102
- 878 Nocquet, J.-M. (2018a). *Pyacs: A set of python tools for gps analysis and tectonic*
879 *modelling*. 19th General Assembly of Wegener.
- 880 Nocquet, J.-M. (2018b). Stochastic static fault slip inversion from geodetic data
881 with non-negativity and bound constraints. *Geophysical Journal International*,
882 214(1), 366–385. doi: 10.1093/gji/ggy146
- 883 Ozener, H., Dogru, A., & Turgut, B. (2013). Quantifying aseismic creep on
884 the ismetpasa segment of the north anatolian fault zone (turkey) by 6
885 years of gps observations. *Journal of Geodynamics*, 67, 72–77. doi:
886 10.1016/j.jog.2012.08.002
- 887 Reid, H. F. (1911). The elastic rebound theory of earthquakes. *Univ. Calif. Publ.*
888 *Bull. Dept. Geol.*, 6, 413–444.
- 889 Rice, J. R. (1992). Fault stress states, pore pressure distributions, and the weak-
890 ness of the san andreas fault. In B. Evans & T.-F. Wong (Eds.), *Fault mechan-*
891 *ics and transport properties in rocks* (p. 475-503). Academic Press.
- 892 Romanet, P., Bhat, H. S., Jolivet, R., & Madariaga, R. (2018). Fast and Slow Slip
893 Events Emerge Due to Fault Geometrical Complexity. *Geophysical Research*

- 894 *Letters*, 45(10), 4809–4819. doi: 10.1029/2018GL077579
- 895 Rouet-Leduc, B., Jolivet, R., Dalaison, M., Johnson, P. A., & Hulbert, C. (2021).
 896 Autonomous extraction of millimeter-scale deformation in insar time se-
 897 ries using deep learning. *Nature Communications*, 12(1), 6480. doi:
 898 10.1038/s41467-021-26254-3
- 899 Rousset, B., Jolivet, R., Simons, M., Lasserre, C., Riel, B., Milillo, P., . . . Renard, F.
 900 (2016). An aseismic slip transient on the North Anatolian Fault. *Geophysical*
 901 *Research Letters*, 43(7), 3254–3262. doi: 10.1002/2016GL068250
- 902 Ruiz, S., Metois, M., Fuenzalida, A., Ruiz, J., Leyton, F., Grandin, R., . . . Cam-
 903 pos, J. (2014). Intense foreshocks and a slow slip event preceded the
 904 2014 Iquique Mw 8.1 earthquake. *Science*, 345(6201), 1165–1169. doi:
 905 10.1126/science.1256074
- 906 Ryder, I., & Bürgmann, R. (2008, December). Spatial variations in slip deficit on
 907 the central San Andreas Fault from InSAR. *Geophysical Journal International*,
 908 175(3), 837–852. doi: 10.1111/j.1365-246X.2008.03938.x
- 909 Savage, J. C., & Burford, R. O. (1973). Geodetic determination of relative plate
 910 motion in central California. *Journal of Geophysical Research*, 78(5), 832–845.
 911 doi: 10.1029/JB078i005p00832
- 912 Scholz, C. H. (1998). Earthquakes and friction laws. *Nature*, 391(6662), 37–42. doi:
 913 10.1038/34097
- 914 Socquet, A., Valdes, J. P., Jara, J., Cotton, F., Walpersdorf, A., Cotte, N., . . . Nor-
 915 abuena, E. (2017). An 8 month slow slip event triggers progressive nucleation
 916 of the 2014 Chile megathrust. *Geophysical Research Letters*, 44(9), 4046–4053.
 917 doi: 10.1002/2017GL073023
- 918 Steinbrugge, K. V., Zacher, E. G., Tocher, D., Whitten, C. A., & Claire, C. N.
 919 (1960). Creep on the San Andreas fault. *Bulletin of the Seismological Society*
 920 *of America*, 50(3), 389–415.
- 921 Sudhaus, H., & Jónsson, S. (2009). Improved source modelling through combined
 922 use of InSAR and GPS under consideration of correlated data errors: appli-
 923 cation to the June 2000 Kleifarvatn earthquake, Iceland. *Geophysical Journal*
 924 *International*, 176(2), 389–404. doi: 10.1111/j.1365-246X.2008.03989.x
- 925 Thomas, M. Y., Avouac, J.-P., Gratier, J.-P., & Lee, J.-C. (2014). Lithologi-
 926 cal control on the deformation mechanism and the mode of fault slip on

- 927 the Longitudinal Valley Fault, Taiwan. *Tectonophysics*, 632, 1–16. doi:
 928 10.1016/j.tecto.2014.05.038
- 929 Thomas, M. Y., Avouac, J.-P., & Lapusta, N. (2017). Rate-and-state friction proper-
 930 ties of the Longitudinal Valley Fault from kinematic and dynamic modeling of
 931 seismic and aseismic slip. *Journal of Geophysical Research-Solid Earth*, 122(4),
 932 3115–3137. doi: 10.1002/2016JB013615
- 933 Wallace, L. M. (2020). Slow slip events in new zealand. *Annual Review of Earth
 934 and Planetary Sciences*, 48(1), 175–203. doi: 10.1146/annurev-earth-071719
 935 -055104
- 936 Wei, M., Kaneko, Y., Liu, Y., & McGuire, J. J. (2013). Episodic fault creep events
 937 in California controlled by shallow frictional heterogeneity. *Nature Geoscience*,
 938 6, 566–570. doi: 10.1038/ngeo1835
- 939 Weiss, J. R., Walters, R. J., Morishita, Y., Wright, T. J., Lazecky, M., Wang, H.,
 940 ... Parsons, B. (2020, 11). High-resolution surface velocities and strain for
 941 anatolia from sentinel-1 insar and gns data. *Geophysical Research Letters*,
 942 47(17), e2020GL087376. doi: 10.1029/2020GL087376
- 943 Williams, S. D. P. (2003). The effect of coloured noise on the uncertainties of rates
 944 estimated from geodetic time series. *Journal of Geodesy*, 76(9-10), 483–494.
 945 doi: 10.1007/s00190-002-0283-4